Received: 13 December 2024 | Revised: 10 April 2025 | Accepted: 20 April 2025

DOI: 10.1002/pro.70152

RESEARCH ARTICLE

THE PROTEIN SOCIETY WILEY

# Phosphorylation of ITIM motifs drives the structural transition of indoleamine 2,3-dioxygenase 1 between enzymatic and non-enzymatic states

Gyula Hoffka[1,2,3] | Lilla Hornyák[2,4] | Lóránt Székvölgyi[4] | Márton Miskei[5,6]

[1]Laboratory of Retroviral Biochemistry, Department of Biochemistry and Molecular Biology, Faculty of Medicine, University of Debrecen, Debrecen, Hungary

[2]Doctoral School of Molecular Cell and Immunobiology, University of Debrecen, Debrecen, Hungary

[3]Department of Chemistry, Lund University, Lund, Sweden

[4]MTA-DE Momentum, Genome Architecture and Recombination Research Group, Department of Molecular and Nanopharmaceutics, Faculty of Pharmacy, University of Debrecen, Debrecen, Hungary

[5]HUN-REN-UD Fungal Stress Biology Research Group, University of Debrecen, Debrecen, Hungary

[6]Department of Molecular Biotechnology and Microbiology, Faculty of Science and Technology, University of Debrecen, Debrecen, Hungary

**Correspondence**
Márton Miskei, HUN-REN-UD Fungal Stress Biology Research Group, University of Debrecen, 4032 Debrecen, Hungary.
Email: miskeim@gmail.com
Lóránt Székvölgyi, MTA-DE Momentum, Genome Architecture and Recombination Research Group, Department of Molecular and Nanopharmaceutics, Faculty of Pharmacy, University of Debrecen, 4032 Debrecen, Hungary.
Email: lorantsz@med.unideb.hu

**Review Editor:** Aitziber L. Cortajarena

## Abstract

Indoleamine 2,3-dioxygenase 1 (IDO1) is the rate-limiting enzyme in tryptophan metabolism that plays a central role in immune regulation across a range of diseases, including cancer. Beyond its enzymatic role, IDO1 has a non-enzymatic function that remains poorly understood. This study explores how phosphorylation of immunoreceptor tyrosine-based inhibitory motifs (ITIMs) modulates IDO1's structural dynamics and functional states. Using molecular dynamics simulations and structural analysis, we show that phosphorylation acts as a molecular switch, inducing conformational changes that regulate heme-binding, remodel specific loop regions, and govern protein–protein interactions with SHP1, SHP2, and SOCS3. Notably, Tyr249 phosphorylation inhibits enzymatic activity by compacting the heme-binding pocket, creating steric hindrance that prevents cofactor binding. In contrast, Tyr111 phosphorylation enhances interactions with SHP1 or SHP2 proteins by embedding their C-terminal regions into the heme-binding pocket, also obstructing heme binding. Furthermore, Tyr249 phosphorylation promotes SOCS3 binding through the formation of a unique loop structure near the phosphorylation site. These findings provide a detailed mechanistic framework for understanding how ITIM phosphorylation orchestrates IDO1's functional transitions, effectively balancing its enzymatic and non-enzymatic functions.

**KEYWORDS**

heme binding, IDO1, immune modulation, immunoreceptor tyrosine-based inhibitory motifs (ITIMs), indoleamine 2,3-dioxygenase 1, molecular dynamics, SHP1, SHP2, SOCS3

## 1 | INTRODUCTION

The human indoleamine 2,3-dioxygenase 1 (IDO1) is a heme-containing enzyme, primarily responsible for the production of kynurenine through the cleavage of the essential amino acid tryptophan (Hornyák et al., 2018). The resulting kynurenine and its downstream metabolites, including 3-hydroxyanthranilic acid (3-HAA), quinolinic acid (QA), and 3-hydroxykynurenine (3-HK), inhibit the proliferation of activated T and B lymphocytes and thereby exert an immunosuppressive effect (Fallarino et al., 2006; Lee et al., 2010; Terness et al., 2002).

Through the kynurenine pathway, IDO1 supports immune tolerance by promoting regulatory T cell (Treg) differentiation, which facilitates tumor cell survival by reducing immune recognition and cytotoxicity of T cells against cancer cells (Acovic et al., 2018; Luu et al., 2017; Matteoli et al., 2010; Munn & Mellor, 2016).

Beyond its enzymatic activity, IDO1 modulates immune responses through non-enzymatic mechanisms that remain to be elucidated. Posttranslational modifications can significantly influence this dual function by altering IDO1's structural stability and/or interactions with cellular signaling pathways. During maturation, removal of the N-terminal methionine from IDO1 generates alanine as the new terminal residue, which is subsequently acetylated (Fujigaki et al., 2006, 2012). This acetylation is thought to contribute to the stabilization of the protein, enhancing its half-life and stability under physiological conditions. Another significant modification is the nitration of three tyrosine residues—Tyr15, Tyr345, and Tyr353—mediated by peroxynitrite, a reactive oxygen species formed during inflammation and oxidative stress (Prolo et al., 2024; Wang et al., 2024). Tyrosine nitration inhibits IDO1's enzymatic activity without affecting its protein levels.

Phosphorylation of other tyrosine residues, such as Tyr111 and Tyr249 in humans (Tyr115 and Tyr253 in mice), further adds complexity to IDO1 regulation. These phosphorylations occur within immunoreceptor tyrosine-based inhibitory motifs (ITIMs), sequences that serve as docking sites for downstream signaling molecules upon phosphorylation (Orabona et al., 2008, 2012; Pallotta et al., 2011). Substituting the ITIM-associated tyrosine residues with phosphomimic glutamic acid demonstrated that ITIM1 phosphorylation facilitates the recruitment of Src homology region 2 domain-containing phosphatases (SHPs). This interaction enables dendritic cells (DCs) to suppress antigen-specific immune responses and enhance immunosuppressive activity in vivo (Albini et al., 2017). SHP1 activation has also been linked to the stimulation of IKKα, a kinase that regulates NF-κB signaling. Specifically, IKKα induces the non-canonical NF-κB pathway by promoting the processing of p100 into p52, leading to the formation of the p52/RelB transcriptional complex, which governs immune and inflammatory responses (Mbongue et al., 2015; Pallotta et al., 2011). There is another study that TGF-β treatment of pDCs leads to phosphorylation of IDO ITIM and formation of a complex between IDO and Shp1 that activates Shp1 phosphatase activity. This is thought to inhibit IRAK1 and activate the non-canonical NF-κB pathway, enhancing type 1 IFN production (Abram & Lowell, 2017). Phosphorylation of ITIM2, on the other hand, recruits suppressor of cytokine signaling 3 (SOCS3), resulting in IDO1 ubiquitination and subsequent proteasomal degradation. Studies employing ITIM2 phosphomimic mutants have highlighted the critical role of SOCS3 in modulating IDO1 signaling and turnover (Albini et al., 2017).

While these findings provide important biological insights, the structural and functional consequences of ITIM phosphorylation remain poorly understood. Structurally, phosphorylation of ITIM tyrosine residues or the presence of phosphomimic glutamate residues likely induces conformational changes that affect IDO1's folding and three-dimensional architecture. These structural rearrangements may impact the enzyme's catalytic site, suggesting that ITIM phosphorylation stabilizes a distinct conformation, separate from the active ligand-bound state of IDO1 (Albini et al., 2017, 2018).

IDO1 predominantly exists in a catalytically inactive apo-form within cells, with an equilibrium between the inactive apoenzyme and active holoenzyme being regulated by intracellular heme availability (Rossini et al., 2024; Salminen, 2022). Phosphorylation of ITIM tyrosine residues, particularly Tyr111 and Tyr249, may further modulate this balance, potentially providing a mechanism to control the enzyme's transition between its distinct functional states.

The disordered JK-loop region (amino acids 360–380) near the heme-binding pocket also plays a regulatory role in IDO1 activity (Sugimoto et al., 2006). This loop exhibits dynamic flexibility, with its C-terminal segment (JK-loopC) adopting closed, intermediate, and open-extended conformations. These structural states either facilitate or restrict substrate access to the catalytic site, depending on the enzyme's functional requirements. In contrast, the N-terminal segment (JK-loopN) remains highly flexible and lacks a defined tertiary structure. In the absence of substrate, the JK-loop predominantly adopts an open conformation, allowing tryptophan to enter the catalytic pocket. Upon substrate binding, the loop transitions to a closed state, stabilized by specific interactions involving Thr379 and Arg231, to support enzymatic activity (Álvarez et al., 2016; Greco et al., 2019). This dynamic conformational flexibility highlights the role of the JK-loop in modulating IDO1 function.

In this study, we investigated the conformational changes and molecular interactions associated with ITIM motif phosphorylation in IDO1. Using molecular modeling, we explored how phosphorylation of ITIM tyrosines influences IDO1's overall conformation, particularly in relation to the architecture of its catalytic pocket. We also examined the conformational dynamics of the JK-loop region and its role in modulating heme accessibility. Our findings reveal that phosphorylation at ITIM2 induces conformational changes that restrict heme accessibility to the catalytic site, likely resulting in the inhibition of enzymatic activity. Furthermore, we found that the phosphorylation state of ITIM tyrosine residues modulates JK-loop dynamics, identifying it as a critical element in regulating IDO1's activity. Based on these results, we propose that ITIM phosphorylation acts as a molecular "switch," allowing IDO1 to transition between its enzymatic and non-enzymatic

states and thereby fine-tuning its molecular function in immune regulation.

## 2 | METHODS

### 2.1 | Heme group parameterization

The parameterization of the IDO1 bound heme cofactor was carried out using the MCPB protocol (Li & Merz, 2016). The two heme propionate groups were modeled in their fully deprotonated (carboxylate) forms, consistent with physiological conditions at neutral pH (~7.0). This protonation state was applied during heme parameterization using the MCPB.py protocol, and was maintained consistently throughout all molecular dynamics simulations. The required small and large systems were built based on the heme-bound IDO1 structure (PDB ID: 6azu) (Nelp et al., 2018), according to the MCPB protocol, with a ferric ($Fe^{3+}$) ion, as according to previous studies such a system is already prone to heme loss (Nelp et al., 2018). Quantum mechanical (QM) calculations, including geometry optimizations, were performed using Gaussian16 software (Frisch et al., 2016), employing the B3LYP method (Becke, 1988, 1993; Lee et al., 1988) and the 6-31G (d) basis set, according to the MCPB protocol. In the case of the small system, in accordance with the protocol, a frequency calculation was also carried out. Final parameterization was carried out with the MCPB.py script provided in AmberTools22 (Case et al., 2023). The parameter files are available at the following Zenodo DOI link: https://doi.org/10.5281/zenodo.15275094

### 2.2 | Protein preparation

The IDO1 structure was prepared using the available crystal structure containing the heme cofactor (PDB ID: 6AZU). Missing residues in the JK-loop (Q361-G320) were modeled using SWISS-MODEL homology modeling software based on the IDO1 sequence (Waterhouse et al., 2018). The protonation states of titratable residues were assigned with PROPKA 3.1 (Olsson et al., 2011; Pettersen et al., 2004; Søndergaard et al., 2011), while neutral histidines were set according to Chimera predictions. Accordingly, Lys375 was modeled in a neutral state. All histidine residues were modeled in a neutral state. Specifically, His45 and His215 were protonated at the Nδ position, while all other histidines were protonated at the Nε position. Parameters for the heme group and coordinating residues (Ala264 and His346) were assigned based on MCPB protocol results. Li/Merz parameters were applied to describe the iron ion. Phosphorylated tyrosine residues of IDO1 were prepared by renaming relevant residues in the PDB file using the ff14SB force field parameter set for phosphorylated residues (Raguette et al., 2024).

### 2.3 | Molecular dynamics protocol

Structure preparation was completed using the tleap script in AmberTools22 (Case et al., 2023), which added missing atoms according to protonation states and incorporated phosphorylated tyrosines. Systems were solvated in a truncated octahedron simulation box with a minimum distance of 12 Å and solvated with TIP3P water molecules (Jorgensen et al., 1983). Physiological NaCl concentration (0.15 M) was achieved by the Split charge protocol (Machado & Pantano, 2020) using the addionsrand command to replace water molecules with sodium and chloride ions while maintaining neutrality. The ff14SB (Maier et al., 2015) force field was applied for protein atoms, and simulations were performed using Amber22 with GPU acceleration (Le Grand et al., 2013; Salomon-Ferrer et al., 2013). The Lennard–Jones parameters for the ferric ion ($Fe^{3+}$) were applied according to the available Amber 12-6-4 LJ-type parameters for a TIP3P water model (Li et al., 2015). The systems were first minimized using the steepest descent method (2500 steps), followed by a conjugate gradient method (7500 steps), with a positional restraint of 10 kcal/mol/$Å^2$ applied to protein heavy atoms. This was followed by heating to 100 K (−173.15°C) in a canonical NVT ensemble during a 250 ps simulation. Systems were heated to 310.15 K (37°C) in an isothermal-isobaric NPT ensemble over 250 ps simulation. The same restraint was applied during the heating steps as well. During the simulations, Langevin dynamics controlled the temperature and the Berendsen barostat maintained pressure (Berendsen et al., 1984). SHAKE constraints were applied to bonds involving hydrogen atoms (Miyamoto & Kollman, 1992). Following heating, further minimization was carried out using the same minimization steps with reduced positional restraints (5 kcal $mol^{-1}$ $Å^{-2}$) on protein heavy atoms. The heating steps were also repeated with the same weakened restraint. Further equilibrations were carried out in NPT ensembles at 310.15 K for six consecutive 100-ps runs each with a decreased positional restraint by 1 kcal $mol^{-1}$ $Å^{-2}$ until the last equilibration, without positional restraints. Final production runs were carried out at 310.15 K for 600 ns using a 2-fs timestep, sampling every 50 ps. For each system, three independent replicas were simulated.

### 2.4 | Analysis of molecular dynamics simulations

Analysis of trajectories was conducted using the cpptraj script from AmberTools22 (Roe & Cheatham, 2013).

Clustering was performed based on the position of Cα atoms using average linkage, with an epsilon value of 4.0 and a sieve number of 10. Distances were calculated between the centers of mass of residues. RMSD was calculated using the standard protocol. For each trajectory, backbone heavy atoms were aligned to the first sampled production structure, carried out based on the backbone heavy atoms, also weighted by mass. Root mean square fluctuation (RMSF) was determined by aligning sampled structures based on Cα atoms outside the region of interest (e.g., in the case of JK-loop calculations, residues outside the JK-loop) and computing fluctuations for these targeted regions.

## 2.5 | Pocket volume analysis

Heme pocket volumes were estimated using POVME 3.0 based on the representative largest cluster of each ensemble (Wagner et al., 2017). The pocket center was defined as the carbonyl oxygen of Ala264, with a radius of 12 Å.

## 2.6 | AlphaFold3 predictions

AlphaFold3 (Abramson et al., 2024) was employed to model interactions between IDO1 (UniProt ID: P14902) and confirmed binding partners SOCS3 (UniProt ID: O14543), SHP1 (UniProt ID: P29350), and SHP2 (UniProt ID: Q06124). Complexes were modeled with and without the heme group for unphosphorylated IDO1, ITIM1-phosphorylated, ITIM2-phosphorylated, and double-phosphorylated forms. To validate the reliability of AlphaFold3 for IDO1 interactions, the AlphaFold3-predicted structure generated from the 6AZU sequence was aligned with the 6AZU crystal structure, with a PyMOL-calculated backbone RMSD of 0.600 Å, indicating excellent structural agreement (Figure S1). The AlphaFold3-predicted SOCS3 in complex with IDO1 (ITIM2-phosphorylated, and double-phosphorylated forms, and also ITIM2-phosphorylated with a removed phosphate group) was prepared and simulated according to the molecular dynamics protocol described in the previous sections, with three simulation replicas and a production run of 300 ns for each replica.

## 2.7 | Statistical analysis

Statistical analyses were conducted using R packages. For RMSD and Ala264-His346 distance calculations, data from three independent simulation replicas were performed, each initiated with distinct random velocity seeds. They were analyzed with 12,000 sampled time points per system. Distances were averaged across replicas at each time point, and 200 randomly selected samples were used for permutation tests involving 10,000 permutations. Observed differences were compared to permuted differences, and *p*-values were calculated to assess statistical significance. In more detail, for each of the 200 randomly sampled points, the average of three data points was calculated for the first sample (e.g., unphosphorylated) and the second sample (e.g., Tyr249 phosphorylated). The difference between these averages was determined for each sampling time point, and the mean of these differences was defined as the observed difference:

$$\text{observed\_diff} = \text{mean}(\text{Tyr249\_means} - \text{unph\_means}).$$

To generate the null distribution, 10,000 random iterations were performed. During each iteration, one sampling time point was randomly selected, and the average values for the two samples were swapped. This swapping was repeated across all sampling points, and the mean difference was recalculated as the permuted difference:

$$\text{permuted\_diff} = \text{mean}(\text{Tyr249\_means} - \text{unph\_means}) \text{ (with swapped averages)}.$$

This permutation approach generated a robust null distribution of permuted differences, allowing for the evaluation of statistical significance by comparing the observed difference against the permuted distribution. In addition, we repeated the permutation test with 200 randomly sampled points 1000 times to determine how many times a significant difference occurred.

In an alternative analysis, 50-bin distributions were constructed from the 12,000 data points, and paired Wilcoxon tests were performed to assess significant differences between the distributions. For RMSF comparisons of the JK-loop dynamics, paired Wilcoxon tests were directly applied without requiring additional smoothing.

# 3 | RESULTS AND DISCUSSION

## 3.1 | Parameterization of the heme cofactor

To accurately model the heme prosthetic group in IDO1, we applied the metal center parameter builder (MCPB) to parameterize the heme group, the iron ion, and the iron-coordinating residues. Although alanine is atypical for metal ion coordination due to its apolar nature, it has been confirmed to coordinate the iron ion via its backbone carbonyl oxygen. We used the 6azu PDB entry (Emamian et al., 2023; Nelp et al., 2018) as the starting structure, which provides evidence for Ala264 coordination in the IDO1 holoenzyme in the absence of a coordinated oxygen molecule or substrate

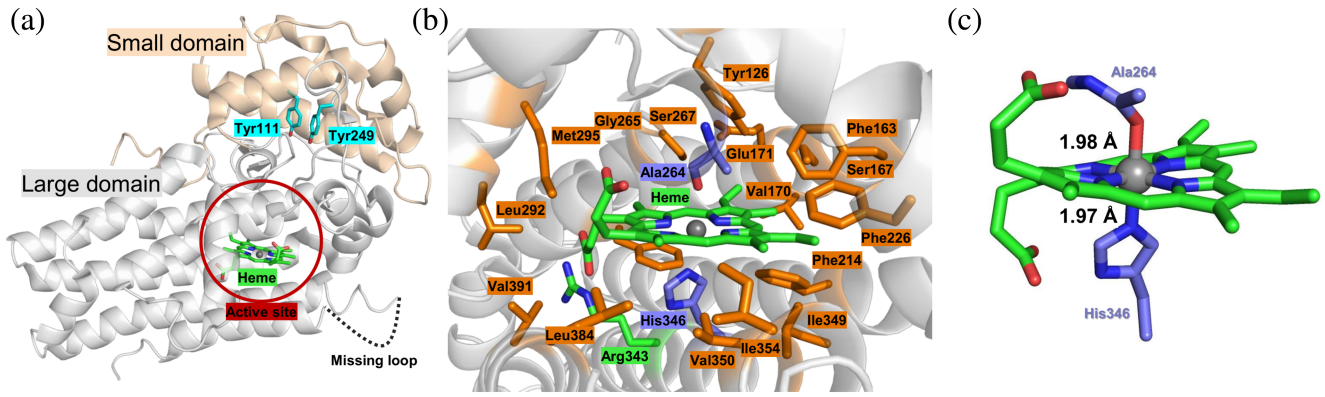


**FIGURE 1** Structural model of IDO1 highlighting the heme-binding pocket and key coordinating residues. (a) The structure of the IDO1 crystal structure (PDB ID: 6AZU). The small and large domains are colored wheat and gray respectively. The Tyr111 (ITIM1) and Tyr249 (ITIM2) residues, central to phosphorylation-mediated regulation, are highlighted with blue sticks. The disordered JK-loop is labeled as "missing loop", as it was not solved in the crystal structure. The heme cofactor, shown in green, is positioned within the active site. (b) Structure of the heme cofactor and its binding residues. The iron ion is represented as a gray sphere, the iron-coordinating residues (Ala264 and His346) are colored purple, the hydrogen bonding residue (Arg343) is colored green and residues involved in apolar interactions are colored orange. The interaction were determined with LigPlot+ (Laskowski & Swindells, 2011). (c) QM/MM optimized structure of the heme cofactor and the iron-coordinating residues (small QM region in the MCPB.py protocol). Distances between the iron ion and the coordinating carbonyl oxygen of Ala264 and ε-nitrogen of His346, highlighting their role in constraining the heme cofactor to the binding pocket.

(Figure 1). Notably, evolutionary analysis indicates that Ala264 is conserved, occupying the equivalent position in the paralogue IDO2 sequence. The parameters derived from this structure (Figure 1) were applied to both the heme group and the coordinating residues, Ala264 and His346, for subsequent simulations and analyses. We note that previous mouse studies demonstrated the essential role of the proximal histidine—His350 in rodents, corresponding to His346 in human IDO1—in coordinating the heme cofactor and sustaining enzymatic activity (Orecchini et al., 2023; Pallotta et al., 2011). While His346 serves as the direct axial ligand to the heme iron, Ala264 appears to play an indirect but supportive role by stabilizing the heme-binding pocket, likely through hydrophobic interactions or backbone coordination, thereby contributing to the structural integrity of the active site.

## 3.2 | Tyr249 phosphorylation or heme binding induces increased flexibility in IDO1

To assess the impact of Tyr249 phosphorylation or heme binding on IDO1's structural stability, molecular dynamics simulations were conducted. Root mean square deviation (RMSD) values were calculated over three independent production runs for each condition, relative to the first frame of the respective run.

In the apo-IDO1 form, the unphosphorylated enzyme exhibited the highest structural stability, as indicated by the lowest RMSD fluctuations (mean RMSD value: 2.27 Å) (Figures S2-S3, blue color, Table S1). By contrast, Tyr249 phosphorylation, either alone or combined with Tyr111 phosphorylation, significantly increased structural fluctuations (paired permutation test, both comparisons in all cases the $p$-value <0.05), reflecting the destabilizing effect of phosphotyrosine modifications. Notably, Tyr111 phosphorylation alone did not induce similar instability.

For the holoenzyme form, RMSD values indicated higher flexibility compared to the apoenzyme, but this was only observed in the unphosphorylated state (Figures S2-S3, red color, Table S1) (paired permutation test, in all cases the $p$-value <0.05). Interestingly, phosphorylation of Tyr111 and Tyr249—individually or in combination—obscured this flexibility difference between holo-IDO1 and apo-IDO1, effectively stabilizing the holoenzyme's structural ensemble. These findings suggest that Tyr249 phosphorylation and heme binding each enhance conformational dynamics in IDO1, with phosphorylation exerting a particularly significant effect in the apoenzyme state.

Next we evaluated the dynamics of the heme-binding-pocket (Figure 2) by measuring distance fluctuations between Ala264 and His346, the key iron-coordinating residues. Phosphorylation at Tyr249 significantly reduced distance fluctuations compared to the unphosphorylated (paired permutation test, out of 1000 replicates 999 had the $p$-value <0.05) or Tyr111-phosphorylated (paired permutation test, in all 1000 replicates the $p$-value <0.05) apoenzyme forms (Figures 2, S4-S5, Table S2). Furthermore, to better explore the conformational dynamics associated with Tyr249 phosphorylation, we performed five independent 1 μs simulations for pTyr249, using the simulated annealing protocols. Based on these extended simulations, we observe a consistent tendency toward closed conformations in the apo form when Tyr249 is

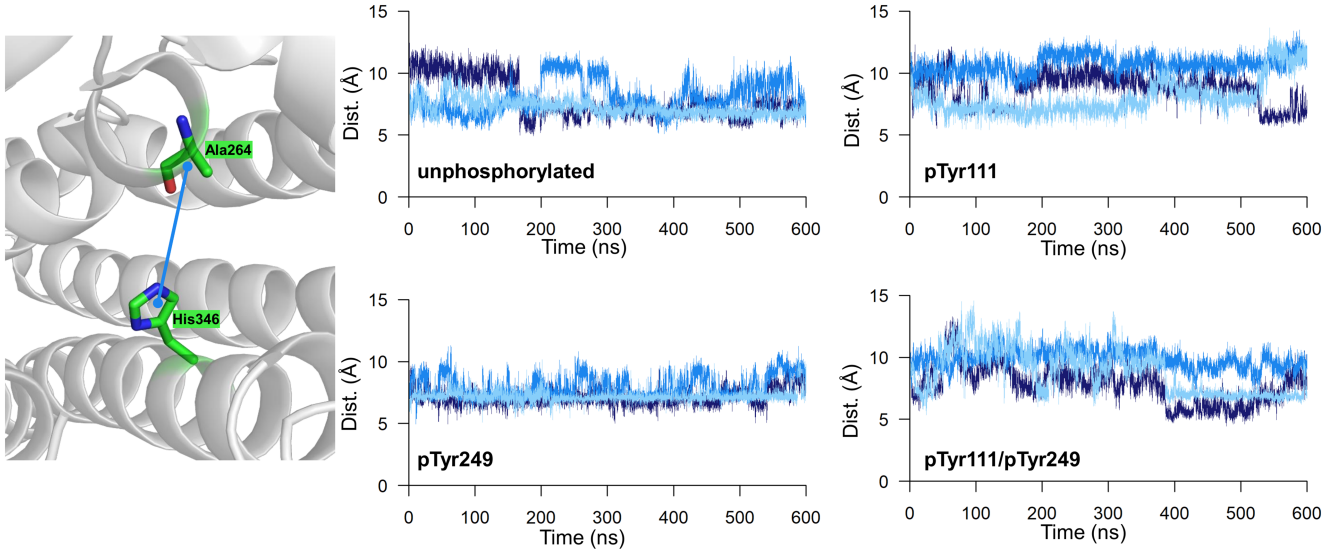


**FIGURE 2** Distance fluctuations between Ala264 and His346 residues, highlighting the effect of Tyr249 phosphorylation on the compactness of the heme-binding pocket in apo-IDO1. The right panel shows that in Tyr249-phosphorylated apo-IDO1, the fluctuation in the distance between these residues is significantly smaller ($p$-value <0.001, paired Wilcoxon test) compared to the values observed in other states.

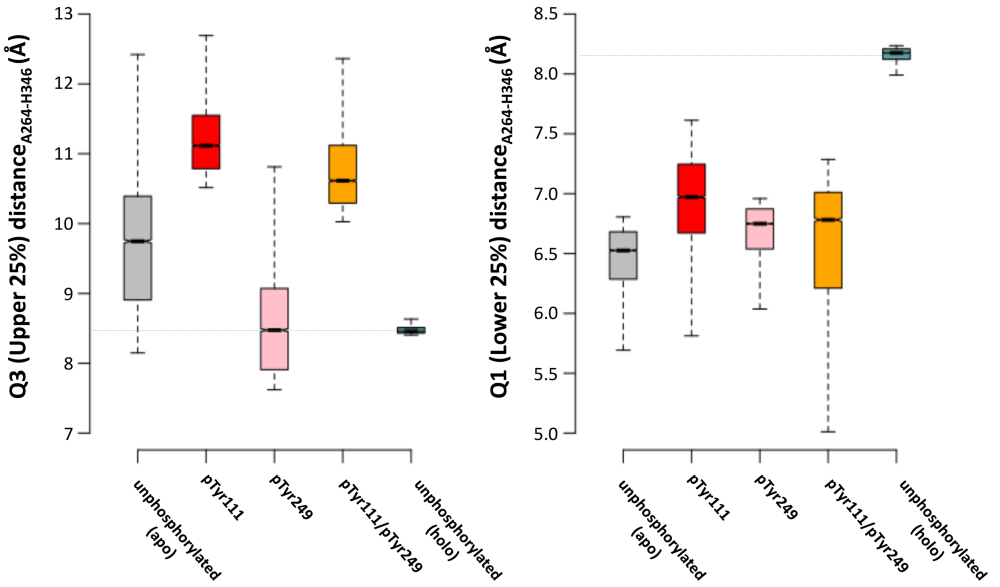


**FIGURE 3** Analysis of distances between Ala264 and His346 residues measured under various phosphorylation states. These residues are the key coordinators of heme binding in IDO1. A total of 12,000 distance measurements were collected over a 600 ns simulation period across three parallel replicates for each phosphorylation state, yielding 36,000 samples per condition. The data were sorted into upper (top 25%) and lower (bottom 25%) percentiles, representing the most open and most compact conformations of the heme-binding pocket, respectively.

phosphorylated. While this finding suggests a reduced likelihood of initial heme binding in the phosphorylated apo form, we acknowledge that this does not entirely preclude heme incorporation, as longer timescales (milliseconds or seconds) may allow rare open-state visits. Moreover, the presence of the heme itself could stabilize open conformations once bound (Figure S6).

Importantly, double phosphorylation at Tyr111 and Tyr249 did not further reduce these fluctuations, indicating that Tyr249 phosphorylation alone is sufficient to stabilize the heme-binding pocket in a compact conformation.

By analyzing the top 25% of distance fluctuations (Q3 percentile, representing open configurations), we observed significantly smaller RMSD values in the Tyr249-phosphorylated form relative to unphosphorylated, Tyr111-phosphorylated, and double-phosphorylated forms (Wilcoxon signed-rank test, $p$-value <0.001; Figure 3). Conversely, in the bottom 25% of fluctuations (Q1 percentile, representing closed configurations), Tyr111-phosphorylated and double-phosphorylated forms exhibited larger RMSD values than the unphosphorylated apoenzyme.

In the holoenzyme form, distance fluctuations remained consistently low (8–8.5 Å) regardless of phosphorylation state, suggesting that the presence of the heme group inherently stabilizes the pocket configuration (Figure S7).

### 3.3 | Pocket volume analysis confirms compaction by Tyr249 phosphorylation

To validate the above findings, we performed pocket volume analyses using POVME software. Tyr249 phosphorylation reduced the pocket volume significantly, from 735 Å$^3$ in the unphosphorylated form to 481 Å$^3$ in the Tyr249-phosphorylated apoenzyme (Figure 4). Double phosphorylation resulted in an intermediate volume (639 Å$^3$), though this reduction did not reach the compactness observed with Tyr249 phosphorylation alone. Interestingly, Tyr111 phosphorylation alone did not substantially affect pocket volume (716 Å$^3$).

These structural changes appear to arise from a groove formation within the heme-binding pocket, induced specifically by Tyr249 phosphorylation (Figure 4). Importantly, this groove was absent in the double-phosphorylated form, further distinguishing the structural effects of single versus combined Tyr phosphorylation events.

Heme pocket volume was also calculated from 100 evenly spaced snapshots per MD trajectory (Figure S8, Table S3). The results obtained from MD measurements confirmed the AlphaFold3 prediction, where the smallest and most compact volume was found in the pTyr249 state.

### 3.4 | Phosphorylation of Tyr249 influences the dynamics of the JK-loop

Using RMSF measurements, we analyzed whether the dynamics of the JK-loop are allosterically influenced by the phosphorylation state of the ITIM motifs. By combining all replicas into a single RMSF profile, the protein's full conformational landscape (sampled over long timescales and independent trajectories) is reflected in the analysis. The JK-loop, which is expected to play a role in modulating substrate and cofactor access to the heme-binding pocket, exhibited distinct dynamics depending on phosphorylation status. In the unphosphorylated apoenzyme (Figure 5, green line), the JK-loop displayed relatively low disorder, maintaining a stable conformation. By contrast, Tyr249 phosphorylation significantly increased the loop's dynamics and conformational heterogeneity (Wilcoxon signed-rank test, *p*-value <0.001) (Figure S9), particularly in regions near the entrance of the heme-

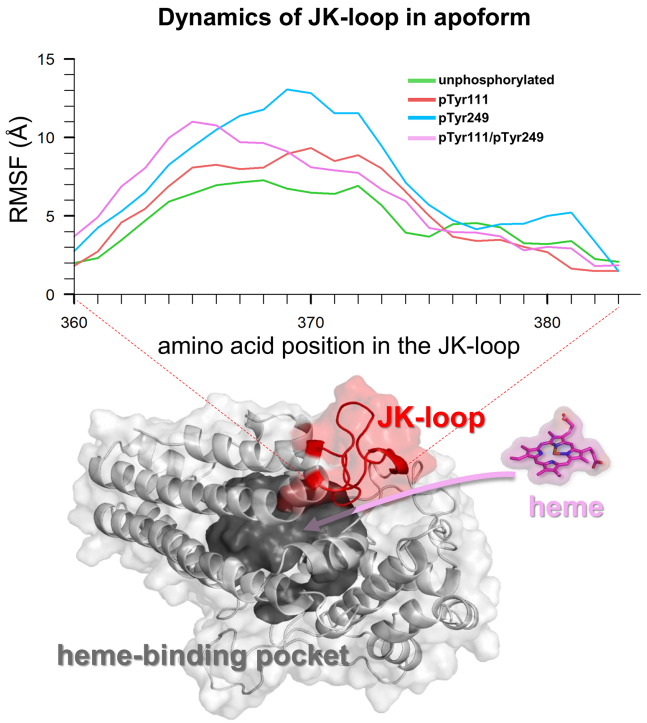


**FIGURE 5** Dynamical states of the JK-loop residues in apo-IDO1. We analyzed the dynamics of the 24 residues forming the JK-loop in apo-IDO1 using root mean square fluctuation (RMSF) measurements. Phosphorylation at Tyr249 in apo-IDO1 resulted in significantly higher fluctuations compared to the unphosphorylated apo-IDO1 (*p*-value <0.01, paired Wilcoxon test) (Figure S6). The lower panel illustrates the position of the JK-loop at the entrance of the heme-binding pocket, suggesting that the increased dynamics observed in the phosphorylated state could prevent heme entry into the pocket.

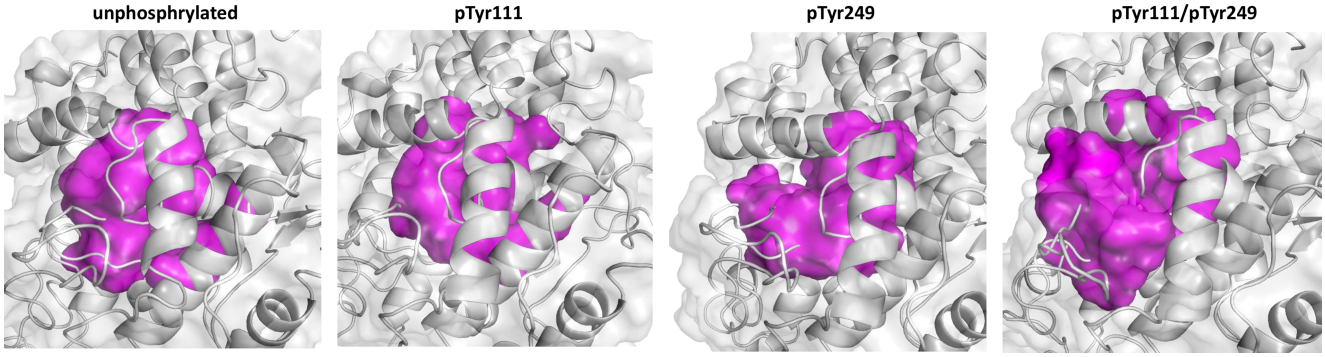


**FIGURE 4** Volume analysis of the heme-binding pocket of IDO1 under different ITIM phosphorylation states. The mean pocket volume significantly decreased in the Tyr249-phosphorylated state compared to the unphosphorylated form. The interior surface of the heme-binding pocket is highlighted in purple.

binding pocket (Figure 5, blue line). This increased mobility aligns with the steric hindrance observed for heme binding, as the JK-loop adopts more obstructive conformations in this state. For Tyr111-phosphorylated and doubly phosphorylated forms (Figure 5, red and purple lines), the JK-loop exhibited intermediate levels of disorder, lying between those of the Tyr249-phosphorylated and unphosphorylated forms. This suggests that Tyr111 phosphorylation stabilizes the JK-loop, though not to the same extent as the unphosphorylated form. Tyr249 phosphorylation appears to override this stabilizing effect, promoting higher loop dynamics and thereby creating a more restrictive environment for heme entry into the pocket.

Interestingly, the JK-loop dynamics were markedly different upon heme binding in the holoenzyme. In the unphosphorylated holo form, the loop exhibited increased flexibility compared to the apoenzyme (Wilcoxon signed-rank test, $p$-value <0.001) (Figure S9). This enhanced flexibility aligns with a previously reported mechanism wherein loop dynamics facilitate the entry of tryptophan into the active site "through" the heme being pre-bound in the pocket (Álvarez et al., 2016; Greco et al., 2019). Thus, the dynamic nature of the JK-loop serves dual roles: while increased disorder in the apo form hinders heme entry, enhanced flexibility in the holo form promotes substrate (tryptophan) access to the catalytic site.

In summary, we found that Tyr249 phosphorylation stimulates JK-loop dynamics, creating a steric barrier to heme binding and stabilizing a closed conformation of the heme-binding pocket. Conversely, the unphosphorylated and Tyr111-phosphorylated forms permit a more open conformation that favors heme accessibility. The structural interplay between loop dynamics, phosphorylation status, and heme binding underscores the regulatory role of JK-loop region in modulating IDO1's functional states.

## 3.5 | Interaction of SHP1 and SHP2 with IDO1

We used AlphaFold3 to model the interactions between IDO1 and the phosphatases SHP1 and SHP2. When SHP1 was modeled with Tyr111-phosphorylated holo-IDO1, the C-terminal alpha-helix of SHP1 was positioned away from the heme-binding pocket, which occupied the heme group (Figure 6a). We note that holo-IDO1 phosphorylated at Tyr249, or doubly phosphorylated at Tyr111 and Tyr249, was not modeled, as our previous analysis showed that Tyr249 phosphorylation prevents heme binding and thus the formation of the holocomplex. In contrast, Tyr111-phosphorylated apo-IDO1 allowed the C-terminal region of SHP1 to wedge into the heme-binding pocket (Figure 6b). This interaction was absent in unphosphorylated, Tyr249 phosphorylated, or Tyr111/Tyr249 doubly phosphorylated apo-IDO1 forms (Figure S10). The structural basis for this difference can be attributed to the effect of Tyr111 phosphorylation, which, according to our structural analysis, causes the pocket to adopt its most open conformational state (Figure 3).

To further explore the spatial relationship between SHP1 and the heme binding pocket, we determined the exact position of the heme in the holoenzyme model and overlaid it with the Tyr111-phosphorylated apo-IDO1–SHP1 complex (Figure 6c). This superimposition clearly demonstrates that the C-terminal region of SHP1 occupies the same site within IDO1 as the heme cofactor, highlighting their mutually exclusive binding. The observed binding of the SHP1 C-terminal tail specifically into the IDO1 heme-binding pocket provides a strong biological validation. Indeed, our results show that this structurally validated interaction occurs exclusively with the apo form of IDO1, specifically in the presence of ITIM1 phosphorylation (Figures 6 and S11).

When SHP2 was modeled with Tyr111-phosphorylated holo-IDO1, its C-terminal tail remained distant from the heme-binding pocket (Figure 7a), similarly to the behavior observed with SHP1 (Figure 6a). Holo-IDO1 phosphorylated at Tyr249 or doubly phosphorylated at Tyr111 and Tyr249 was not included in the analysis, as Tyr249 phosphorylation has been shown to block heme binding and prevent holocomplex formation. In contrast, Tyr111-phosphorylated apo-IDO1 allowed the C-terminal tail of SHP2 to wedge into the heme-binding pocket (Figure 7b). Unlike SHP1, SHP2 does not adopt an alpha-helical secondary structure during this interaction. Overlaying the position of heme with the Tyr111-phosphorylated apo-IDO1–SHP2 complex revealed that the C-terminal region of SHP2 occupies the same site as the heme cofactor within IDO1 (Figure 7c). When IDO1 is doubly phosphorylated on Tyr111/Tyr249, its interaction with SHP2 does not result in the insertion of the C-terminal tail into the heme-binding pocket (Figure S12). In none of the holo-IDO1 forms was it observed that the C-terminal tail of the SHP1 or SHP2 proteins was bound into the IDO1 heme-binding pocket. These models support the conclusion that C-terminal binding of SHP1/2 requires an open, heme-free (apo) conformation of IDO1 (Figure S13).

## 3.6 | SOCS3 interaction with IDO1

We also modeled the interaction of IDO1 with the SOCS3 protein using AlphaFold3. The predictions indicate that phosphorylation of Tyr249 (ITIM2) facilitates the interaction with SOCS3. This interaction appears to be mediated by a loop structure that forms near Tyr249 on IDO1, which develops exclusively in the presence of SOCS3. Notably, this loop structure is absent when SOCS3 is not bound to IDO1.

In the predicted IDO1–SOCS3 interaction model, an ionic bond is observed between Glu254 and Arg109,

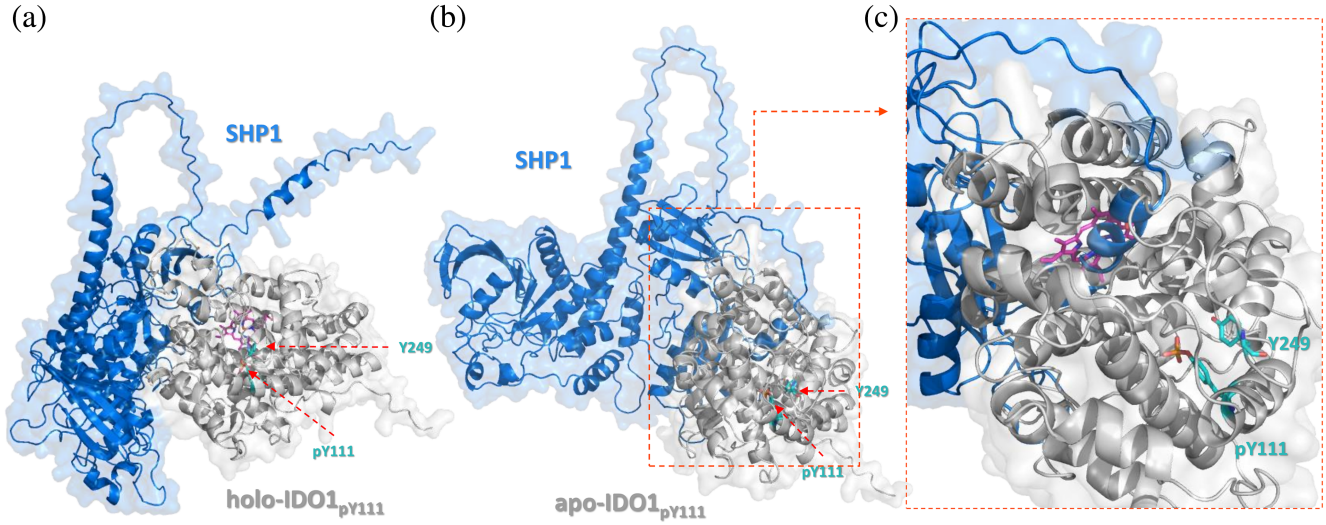


**FIGURE 6** Interactions of Tyr111-phosphorylated IDO1 and SHP1 predicted by AlphaFold3. The interactions vary depending on whether IDO1 is in its holoenzyme or apoenzyme form. Tyr111 (phosphorylated) and Tyr249 (unphosphorylated) are depicted in stick representation. (a) In the holoenzyme, the C-terminal alpha-helix of SHP1 is positioned away from the heme-binding pocket, which accommodates the heme group. (b) In the apoenzyme, the C-terminal region of SHP1 engages with the heme-binding pocket. (c) The position of the heme group is superimposed onto the SHP1-bound apo-IDO1pTyr111 complex. The inserted alpha-helix formed by the C-terminal region of SHP1 coincides with the heme cofactor (shown in purple).

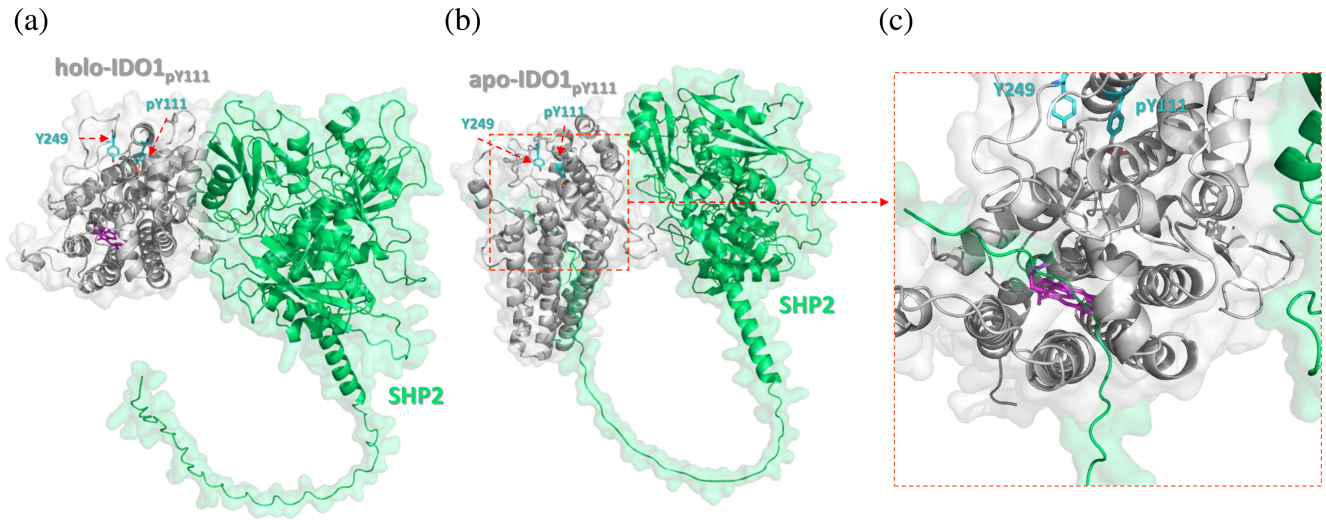


**FIGURE 7** Interactions of Tyr111-phosphorylated IDO1 and SHP2 predicted by AlphaFold3. The interactions differ depending on whether IDO1 is in its holoenzyme or apoenzyme form. Phosphorylated Tyr111 and unphosphorylated Tyr249 are shown in stick representation. (a) In the holoenzyme, the C-terminal tail of SHP2 remains distant from the heme-binding pocket. (b) In the apoenzyme, the C-terminal region of SHP2 interacts with the heme-binding pocket. (c) The position of the heme group is superimposed onto the SHP2-bound apo-IDO1pTyr111 complex. In this state, the C-terminal region of SHP2 overlaps with the heme cofactor (shown in purple).

with a bond distance of less than 2 Å (Figure 8e). Additionally, the phosphate group of pTyr249 participates in the formation of the interaction loop with an additional ionic bond (pTyr249-Arg71) and two hydrogen bonds (pTyr249-Ser73 and pTyr249-Ser74), further stabilizing the interaction between IDO1 and SOCS3. Interestingly, in the Tyr111/Tyr249 double-phosphorylated form of IDO1, the loop structure near Tyr249 remains intact; the ionic bond between Glu254 and Arg109 is no longer present. Instead, Glu254 of IDO1 rotates away, increasing the distance between the two side chains to over 8 Å (Figure 8f). We confirmed our observations with several AlphaFold3 replicates (Table S4) and validated the change in distance between the Glu254 and Arg109 residues in the two states (ITIM2 or ITIM1/ITIM2 phosphorylation) through MD simulations (Table S5). Furthermore, the MD simulations showed that the ionic bond disappeared when the pTyr249

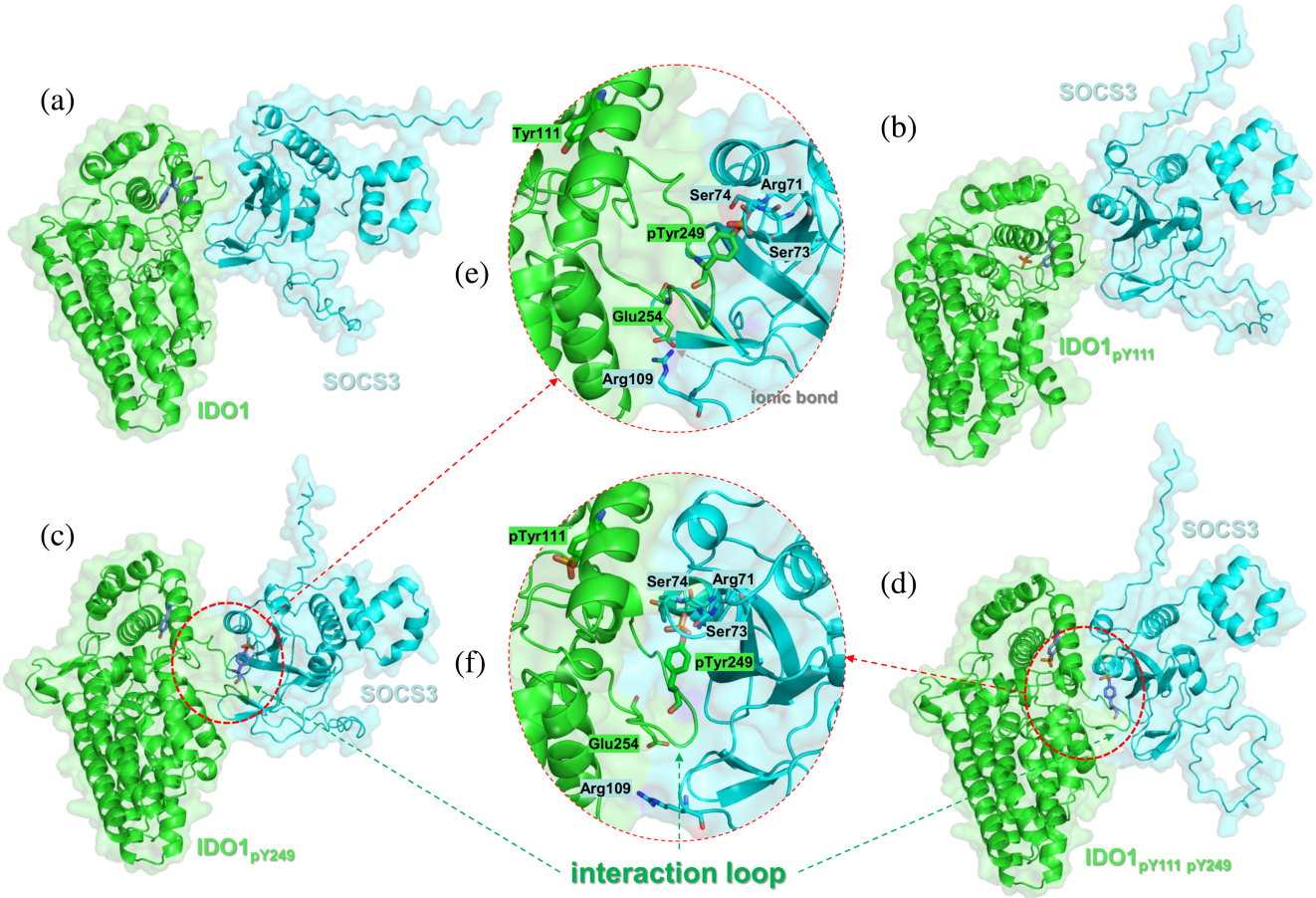


**FIGURE 8** Interactions of apo-IDO1 and SOCS3 predicted by AlphaFold3. IDO1 is shown in green, and SOCS3 is depicted in cyan. AlphaFold3 predicted SOCS3 interactions with (a) unphosphorylated IDO1, (b) Tyr111-phosphorylated IDO1, (c) Tyr249-phosphorylated IDO1, and (d) Tyr111/Tyr249 double-phosphorylated IDO1. A loop structure forms on the interaction surface in the Tyr249-phosphorylated and Tyr111/Tyr249 double-phosphorylated forms. (e) Interaction loop (ionic bond) between SOCS3 and apo-IDO1. In Tyr249-phosphorylated IDO1, Arg109 of SOCS3 and Glu254 of IDO1 align within 2 Å, suggesting the formation of a potential ionic bond. (f) Absence of ionic bond between SOCS3 and apo-IDO1. In Tyr111/Tyr249 double-phosphorylated IDO1, the distance between Arg109 of SOCS3 and Glu254 of IDO1 increases to approximately 8 Å, indicating that the ionic bond is likely not formed under these conditions. (e and f) In the case of the phosphorylated Tyr249 and the Tyr111/Tyr249 double-phosphorylated apo-IDO1, the pTyr phosphate group further stabilizes the loop with three additional bonds: An ionic interaction between pTyr249 and Arg71, and hydrogen bonds between pTyr249 and Ser73, as well as between pTyr249 and Ser74 of SOCS3.

phosphate group was removed from the ITIM2-phosphorylated apo-IDO1. This confirms that ITIM2 phosphorylation plays a role in the formation of the conformation in which an ionic bond is established between Glu254 and Arg109 (Table S5).

These structural rearrangements align with experimental data on ITIM motif phosphorylation and its effects on IDO1 protein stability (Albini et al., 2017). According to these studies, IDO1 degradation occurs even when both Tyr111 and Tyr249 are phosphorylated, although the rate of degradation is reduced compared to the form where only Tyr249 is phosphorylated (Albini et al., 2017). This suggests that ITIM motif phosphorylation dynamically modulates IDO1's interaction with SOCS3 and its subsequent stability.

In a previous study, Mondanelli and colleagues demonstrated that, in a K257E IDO1 mutant, the mutation led to an increased rate of IDO1 degradation (Mondanelli et al., 2020). Based on this, we performed an AlphaFold3 simulation with a K257E mutant ITIM2-phosphorylated apo-IDO1 and SOCS3 complex to examine the changes in the interaction loop (Figure S14). The mutation did not eliminate the interaction loop; however, it increased the distance between the Glu254 and Arg109 residues. Thus, it can be assumed that as a result of the mutation, the aforementioned salt bridge disappeared but was compensated by the formation of a hydrogen bond (stronger than the salt bridge) between the residues of IDO1 K257E and SOCS3 Gly51. This newly formed secondary bond resulted in a much more stable interaction loop, which accounts for the accelerated degradation of IDO1. The distances of the bonds formed by pTyr249 do not change here either, so they participate in the formation of the loop.

## 4 | CONCLUSIONS

In this study, we explored the structural and functional implications of ITIM motif phosphorylation on IDO1, revealing how these modifications regulate the enzyme's transition between distinct functional states, potentially governing its enzymatic and non-enzymatic roles. Our results show that phosphorylation at ITIM2 (Tyr249) appears to significantly reduce, but not necessarily prevent, heme binding through a combination of structural compaction and increased JK-loop dynamics. Tyr249 phosphorylation reduces the heme-binding pocket volume, stabilizes a closed-pocket conformation, and increases disorder in the JK-loop region, which collectively hinder heme accessibility. By contrast, unphosphorylated and Tyr111-phosphorylated forms maintain an open-pocket conformation, facilitating heme entry. Interestingly, holo-IDO1's structural flexibility is inherently stabilized by the presence of the heme group, but this stabilization is overridden by Tyr249 phosphorylation in the apoenzyme, which locks the pocket in a closed state.

Phosphorylation of ITIM1 (Tyr111), on the other hand, induces conformational changes that promote interactions with SHP1 and SHP2. Tyr111 phosphorylation allows the C-terminal tail of SHPs to embed into the heme-binding pocket, an interaction facilitated by the open-pocket conformation induced by this phosphorylation. This helix-in-groove interaction also strengthens the likelihood of the IDO1–SHP1/2 interactions. As such a structural feature has never been observed in any known complex involving IDO1 or SHP1/2 as one or both interaction partners, it is inconceivable that its formation is merely the result of misleading training of AlphaFold3. Moreover, the legitimacy of this structure is reinforced by the fact that this motif appears exclusively in one form—specifically, in ITIM1-phosphorylated apo-IDO1—for both SHP1 and SHP2. However, in the doubly phosphorylated state (Tyr111 and Tyr249), pocket closure driven by Tyr249 phosphorylation disrupts SHP1 and SHP2 interactions. This dual regulatory mechanism segregates IDO1's roles: enabling SHP-driven immunosuppressive signaling when singly phosphorylated at Tyr111 and promoting SOCS3-mediated proteasomal degradation when doubly phosphorylated.

The interaction between SOCS3 and phosphorylated Tyr249 further underscores the complexity of IDO1 regulation. Tyr249 phosphorylation facilitates the formation of a loop structure on the interaction surface, which is absent without SOCS3. This loop mediates SOCS3 binding, stabilized by ionic and hydrogen bonds, although this interaction weakens in the Tyr111/Tyr249 doubly phosphorylated state due to the loss of a critical ionic bond. These findings align with experimental evidence suggesting that Tyr249 phosphorylation promotes IDO1 degradation, albeit at a reduced rate when both ITIM motifs are phosphorylated. In addition, our MD studies confirmed that the pTyr249 phosphate group is critically important for the formation and stabilization of the interaction loop, because its removal causes the interactions stabilizing the loop among the participating residues to vanish as they drift apart, and presumably with the disappearance of the interaction loop, degradation initiation also fails.

Overall, our results establish ITIM motifs as molecular switches that dictate IDO1's functional state. Depending on their phosphorylation status, these motifs regulate the enzyme's structural dynamics, interactions with SHPs and SOCS3, and enzymatic activity. This mechanistic framework highlights how phosphorylation-driven conformational changes enable IDO1 to balance its enzymatic and non-enzymatic functions, supporting its role in immune regulatory processes.

## AUTHOR CONTRIBUTIONS

**Gyula Hoffka:** Conceptualization; investigation; writing – original draft; methodology; visualization; software; data curation. **Lilla Hornyák:** Writing – review and editing. **Lóránt Székvölgyi:** Writing – review and editing; writing – original draft; supervision. **Márton Miskei:** Supervision; conceptualization; investigation; funding acquisition; writing – original draft; visualization; writing – review and editing; validation; formal analysis.

## ACKNOWLEDGMENTS

This research was supported by the National Research, Development and Innovation Office (Hungary) projects NKFIH-K-137678, NKFIH-K-142137, and the Thematic Excellence Programme TKP2021-EGA-18 implemented with the support provided by the Ministry of Culture and Innovation of Hungary financed under the TKP2021-EGA and TKP2021EGA funding schemes. We acknowledge KIFÜ for awarding us access to resources (Komondor) based in Hungary. MM's salary is provided by HUN-REN Hungarian Research Network.

## DATA AVAILABILITY STATEMENT

The data that support the findings of this study are available from the corresponding author upon reasonable request.

## ORCID

*Márton Miskei* https://orcid.org/0000-0002-8272-0006

## REFERENCES

Abram CL, Lowell CA. Shp1 function in myeloid cells. J Leukoc Biol. 2017;102(3):657–75. https://doi.org/10.1189/jlb.2MR0317-105R

Abramson J, Adler J, Dunger J, Evans R, Green T, Pritzel A, et al. Accurate structure prediction of biomolecular interactions with AlphaFold 3. Nature. 2024;630(8016):493–500. https://doi.org/10.1038/s41586-024-07487-w

Acovic A, Gazdic M, Jovicic N, Harrell CR, Fellabaum C, Arsenijevic N, et al. Role of indoleamine 2,3-dioxygenase in

pathology of the gastrointestinal tract. Therap Adv Gastroenterol. 2018;11:1756284818815334. https://doi.org/10.1177/1756284818815334

Albini E, Rosini V, Gargaro M, Mondanelli G, Belladonna ML, Pallotta MT, et al. Distinct roles of immunoreceptor tyrosine-based motifs in immunosuppressive indoleamine 2,3-dioxygenase 1. J Cell Mol Med. 2017;21(1):165–76. https://doi.org/10.1111/jcmm.12954

Albini E, Coletti A, Greco F, Pallotta MT, Mondanelli G, Gargaro M, et al. Identification of a 2-propanol analogue modulating the non-enzymatic function of indoleamine 2,3-dioxygenase 1. Biochem Pharmacol. 2018;158:286–97. https://doi.org/10.1016/j.bcp.2018.10.033

Álvarez L, Lewis-Ballester A, Roitberg A, Estrin DA, Yeh S-R, Marti MA, et al. Structural study of a flexible active site loop in human indoleamine 2,3-dioxygenase and its functional implications. Biochemistry. 2016;55(19):2785–93. https://doi.org/10.1021/acs.biochem.6b00077

Becke AD. Density-functional exchange-energy approximation with correct asymptotic behavior. Phys Rev A. 1988;38(6):3098–100. https://doi.org/10.1103/PhysRevA.38.3098

Becke AD. Density-functional thermochemistry. III. The role of exact exchange. J Chem Phys. 1993;98(7):5648–52. https://doi.org/10.1063/1.464913

Berendsen HJC, Postma JPM, Van Gunsteren WF, DiNola A, Haak JR. Molecular dynamics with coupling to an external Bath. J Chem Phys. 1984;81(8):3684–90. https://doi.org/10.1063/1.448118

Case DA, Aktulga HM, Belfon K, Cerutti DS, Cisneros GA, Cruzeiro VWD, et al. AmberTools. J Chem Inf Model. 2023;63(20):6183–91. https://doi.org/10.1021/acs.jcim.3c01153

Emamian S, Ireland KA, Purohit V, McWhorter KL, Maximova O, Allen W, et al. X-ray emission spectroscopy of single protein crystals yields insights into heme enzyme intermediates. J Phys Chem Lett. 2023;14(1):41–8. https://doi.org/10.1021/acs.jpclett.2c03018

Fallarino F, Grohmann U, You S, McGrath BC, Cavener DR, Vacca C, et al. The combined effects of tryptophan starvation and tryptophan catabolites down-regulate T cell receptor ζ-chain and induce a regulatory phenotype in naive T cells. J Immunol. 2006;176(11):6752–61. https://doi.org/10.4049/jimmunol.176.11.6752

Frisch MJ, Trucks GW, Schlegel HB, Scuseria GE, Robb MA, Cheeseman JR, et al. Gaussian 16 Revision C.01. 2016. https://gaussian.com/citation/

Fujigaki H, Saito K, Lin F, Fujigaki S, Takahashi K, Martin BM, et al. Nitration and inactivation of IDO by peroxynitrite. J Immunol. 2006;176(1):372–9. https://doi.org/10.4049/jimmunol.176.1.372

Fujigaki H, Seishima M, Saito K. Posttranslational modification of indoleamine 2,3-dioxygenase. Anal Bioanal Chem. 2012;403(7):1777–82. https://doi.org/10.1007/s00216-012-5946-2

Greco FA, Albini E, Coletti A, Dolciami D, Carotti A, Orabona C, et al. Tracking hidden binding pockets along the molecular recognition path of l -Trp to indoleamine 2,3-dioxygenase 1. ChemMedChem. 2019;14(24):2084–92. https://doi.org/10.1002/cmdc.201900529

Hornyák L, Dobos N, Koncz G, Karányi Z, Páll D, Szabó Z, et al. The role of indoleamine-2,3-dioxygenase in cancer development, diagnostics, and therapy. Front Immunol. 2018;9:151. https://doi.org/10.3389/fimmu.2018.00151

Jorgensen WL, Chandrasekhar J, Madura JD, Impey RW, Klein ML. Comparison of simple potential functions for simulating liquid water. J Chem Phys. 1983;79(2):926–35. https://doi.org/10.1063/1.445869

Laskowski RA, Swindells MB. LigPlot+: multiple ligand–protein interaction diagrams for drug discovery. J Chem Inf Model. 2011;51(10):2778–86. https://doi.org/10.1021/ci200227u

Le Grand S, Götz AW, Walker RC. SPFP: speed without compromise—a mixed precision model for GPU accelerated molecular dynamics simulations. Comput Phys Commun. 2013;184(2):374–80. https://doi.org/10.1016/j.cpc.2012.09.022

Lee C, Yang W, Parr RG. Development of the Colle-Salvetti correlation-energy formula into a functional of the electron density. Phys Rev B. 1988;37(2):785–9. https://doi.org/10.1103/PhysRevB.37.785

Lee S-M, Lee Y-S, Choi J-H, Park S-G, Choi I-W, Joo Y-D, et al. Tryptophan metabolite 3-hydroxyanthranilic acid selectively induces activated T cell death via intracellular GSH depletion. Immunol Lett. 2010;132(1–2):53–60. https://doi.org/10.1016/j.imlet.2010.05.008

Li P, Merz KM. MCPB.Py: a python based metal center parameter builder. J Chem Inf Model. 2016;56(4):599–604. https://doi.org/10.1021/acs.jcim.5b00674

Li P, Song LF, Merz KM. Parameterization of highly charged metal ions using the 12-6-4 LJ-type nonbonded model in explicit water. J Phys Chem B. 2015;119(3):883–95. https://doi.org/10.1021/jp505875v

Luu M, Steinhoff U, Visekruna A. Functional heterogeneity of gut-resident regulatory T cells. Clin Transl Immunol. 2017;6(9):e156. https://doi.org/10.1038/cti.2017.39

Machado MR, Pantano S. Split the charge difference in two! A rule of thumb for adding proper amounts of ions in MD simulations. J Chem Theory Comput. 2020;16(3):1367–72. https://doi.org/10.1021/acs.jctc.9b00953

Maier JA, Martinez C, Kasavajhala K, Wickstrom L, Hauser KE, Simmerling C. ff14SB: improving the accuracy of protein side chain and backbone parameters from ff99SB. J Chem Theory Comput. 2015;11(8):3696–713. https://doi.org/10.1021/acs.jctc.5b00255

Matteoli G, Mazzini E, Iliev ID, Mileti E, Fallarino F, Puccetti P, et al. Gut CD103+ dendritic cells express indoleamine 2,3-dioxygenase which influences T regulatory/T effector cell balance and oral tolerance induction. Gut. 2010;59(5):595–604. https://doi.org/10.1136/gut.2009.185108

Mbongue J, Nicholas D, Torrez T, Kim N-S, Firek A, Langridge W. The role of indoleamine 2,3-dioxygenase in immune suppression and autoimmunity. Vaccine. 2015;3(3):703–29. https://doi.org/10.3390/vaccines3030703

Miyamoto S, Kollman PA. Settle: an analytical version of the SHAKE and RATTLE algorithm for rigid water models. J Comput Chem. 1992;13(8):952–62. https://doi.org/10.1002/jcc.540130805

Mondanelli G, Di Battista V, Pellanera F, Mammoli A, Macchiarulo A, Gargaro M, et al. A novel mutation of indoleamine 2,3-dioxygenase 1 causes a rapid proteasomal degradation and compromises protein function. J Autoimmun. 2020;115:102509. https://doi.org/10.1016/j.jaut.2020.102509

Munn DH, Mellor AL. IDO in the tumor microenvironment: inflammation, counter-regulation, and tolerance. Trends Immunol. 2016;37(3):193–207. https://doi.org/10.1016/j.it.2016.01.002

Nelp MT, Kates PA, Hunt JT, Newitt JA, Balog A, Maley D, et al. Immune-modulating enzyme indoleamine 2,3-dioxygenase is effectively inhibited by targeting its apo-form. Proc Natl Acad Sci. 2018;115(13):3249–54. https://doi.org/10.1073/pnas.1719190115

Olsson MHM, Søndergaard CR, Rostkowski M, Jensen JH. PROPKA3: consistent treatment of internal and surface residues in empirical pKa predictions. J Chem Theory Comput. 2011;7(2):525–37. https://doi.org/10.1021/ct100578z

Orabona C, Pallotta MT, Volpi C, Fallarino F, Vacca C, Bianchi R, et al. SOCS3 drives proteasomal degradation of indoleamine 2,3-dioxygenase (IDO) and antagonizes IDO-dependent tolerogenesis. Proc Natl Acad Sci. 2008;105(52):20828–33. https://doi.org/10.1073/pnas.0810278105

Orabona C, Pallotta MT, Grohmann U. Different partners, opposite outcomes: a new perspective of the immunobiology of

indoleamine 2,3-dioxygenase. Mol Med. 2012;18(5):834–42. https://doi.org/10.2119/molmed.2012.00029
Orecchini E, Belladonna ML, Pallotta MT, Volpi C, Zizi L, Panfili E, et al. The signaling function of IDO1 incites the malignant progression of mouse B16 melanoma. Oncoimmunology. 2023;12(1): 2170095. https://doi.org/10.1080/2162402X.2023.2170095
Pallotta MT, Orabona C, Volpi C, Vacca C, Belladonna ML, Bianchi R, et al. Indoleamine 2,3-dioxygenase is a signaling protein in long-term tolerance by dendritic cells. Nat Immunol. 2011; 12(9):870–8. https://doi.org/10.1038/ni.2077
Pettersen EF, Goddard TD, Huang CC, Couch GS, Greenblatt DM, Meng EC, et al. UCSF chimera—a visualization system for exploratory research and analysis. J Comput Chem. 2004; 25(13):1605–12. https://doi.org/10.1002/jcc.20084
Prolo C, Piacenza L, Radi R. Peroxynitrite: a multifaceted oxidizing and nitrating metabolite. Curr Opin Chem Biol. 2024;80:102459. https://doi.org/10.1016/j.cbpa.2024.102459
Raguette LE, Cuomo AE, Belfon KAA, Tian C, Hazoglou V, Witek G, et al. phosaa14SB and phosaa19SB: updated Amber force field parameters for phosphorylated amino acids. J Chem Theory Comput. 2024;20(16):7199–209, acs.jctc.4c00732. https://doi.org/10.1021/acs.jctc.4c00732
Roe DR, Cheatham TE. PTRAJ and CPPTRAJ: software for processing and analysis of molecular dynamics trajectory data. J Chem Theory Comput. 2013;9(7):3084–95. https://doi.org/10.1021/ct400341p
Rossini S, Ambrosino S, Volpi C, Belladonna ML, Pallotta MT, Panfili E, et al. Epacadostat stabilizes the apo-form of IDO1 and signals a pro-tumorigenic pathway in human ovarian cancer cells. Front Immunol. 2024;15:1346686. https://doi.org/10.3389/fimmu.2024.1346686
Salminen A. Role of indoleamine 2,3-dioxygenase 1 (IDO1) and kynurenine pathway in the regulation of the aging process. Ageing Res Rev. 2022;75:101573. https://doi.org/10.1016/j.arr.2022.101573
Salomon-Ferrer R, Götz AW, Poole D, Le Grand S, Walker RC. Routine microsecond molecular dynamics simulations with AMBER on GPUs. 2. Explicit solvent particle mesh Ewald. J Chem Theory Comput. 2013;9(9):3878–88. https://doi.org/10.1021/ct400314y
Søndergaard CR, Olsson MHM, Rostkowski M, Jensen JH. Improved treatment of ligands and coupling effects in empirical calculation and rationalization of pKa values. J Chem Theory Comput. 2011;7(7):2284–95. https://doi.org/10.1021/ct200133y
Sugimoto H, Oda S, Otsuki T, Hino T, Yoshida T, Shiro Y. Crystal structure of human indoleamine 2,3-dioxygenase: catalytic mechanism of O2 incorporation by a heme-containing dioxygenase. Proc Natl Acad Sci. 2006;103(8):2611–6. https://doi.org/10.1073/pnas.0508996103
Terness P, Bauer TM, Röse L, Dufter C, Watzlik A, Simon H, et al. Inhibition of allogeneic T cell proliferation by indoleamine 2,3-dioxygenase—expressing dendritic cells. J Exp Med. 2002; 196(4):447–57. https://doi.org/10.1084/jem.20020052
Wagner JR, Sørensen J, Hensley N, Wong C, Zhu C, Perison T, et al. POVME 3.0: software for mapping binding pocket flexibility. J Chem Theory Comput. 2017;13(9):4584–92. https://doi.org/10.1021/acs.jctc.7b00500
Wang B, Kong Y, Tian X, Xu M. A highly sensitive and selective chemiluminescent probe for peroxynitrite detection in vitro, in vivo and in human liver cancer tissue. J Hazard Mater. 2024; 469:134094. https://doi.org/10.1016/j.jhazmat.2024.134094
Waterhouse A, Bertoni M, Bienert S, Studer G, Tauriello G, Gumienny R, et al. SWISS-MODEL: homology modelling of protein structures and complexes. Nucleic Acids Res. 2018;46(W1): W296–303. https://doi.org/10.1093/nar/gky427

## SUPPORTING INFORMATION

Additional supporting information can be found online in the Supporting Information section at the end of this article.

**How to cite this article:** Hoffka G, Hornyák L, Székvölgyi L, Miskei M. Phosphorylation of ITIM motifs drives the structural transition of indoleamine 2,3-dioxygenase 1 between enzymatic and non-enzymatic states. Protein Science. 2025;34(6):e70152. https://doi.org/10.1002/pro.70152